




Article

An Efficient Inverse Synthetic Aperture Imaging Approach for Non-Cooperative Space Targets under Low-Signal-to-Noise-Ratio Conditions

Zhijun Yang ^{1,2} , Chengxiang Zhang ^{1,*} , Dujuan Liang ³ and Xin Xie ² 

¹ Chongqing Innovation Center, Beijing Institute of Technology, Chongqing 401120, China; yangzj158@cqu.edu.cn

² Radar Research Lab, School of Information and Electronics, Beijing Institute of Technology, Beijing 100811, China; 3120215409@bit.edu.cn

³ Communication Sergeant School, PLA Army Engineering University, Chongqing 400035, China; heqingche@cqu.edu.cn

* Correspondence: chengxiangz1993@alu.cqu.edu.cn

Abstract: Due to the non-cooperative characteristics of space targets with complex motion, it is difficult to obtain high-quality inverse synthetic aperture (ISAR) images using conventional imaging approaches, posing a new challenge when designing novel approaches, especially under low-signal-to-noise-ratio (SNR) conditions. To overcome the obstacle above, in this work, an efficient ISAR imaging approach based on high-order synchrosqueezing transform and modified multi-scale retinex (HSTMMSR) is proposed. First, the geometry and signal model of non-cooperative space targets with complex motion are established. Second, the echoes in each range bin are modeled as multi-component polynomial phase signals (MCPPSs) after correcting the translational migration and migration through range cells (MTRCs). Additionally, the time–frequency analysis (TFA) method based on HoSST is utilized to generate the time–frequency signal along with the azimuth dimension, where the coarse ISAR image is obtained with the quality indicator, e.g., image entropy, followed by the MMSR method to enhance the result. Both the simulated and measured data experiments validate the effectiveness and robustness of the proposed method.

Keywords: inverse synthetic aperture radar (ISAR) imaging; HSTMMSR; non-cooperative space targets



Citation: Yang, Z.; Zhang, C.; Liang, D.; Xie, X. An Efficient Inverse Synthetic Aperture Imaging Approach for Non-Cooperative Space Targets under Low-Signal-to-Noise-Ratio Conditions. *Electronics* **2023**, *12*, 4527. <https://doi.org/10.3390/electronics12214527>

Academic Editor:
Massimiliano Pieraccini

Received: 21 September 2023
Revised: 23 October 2023
Accepted: 24 October 2023
Published: 3 November 2023



Copyright: © 2023 by the authors. Licensee MDPI, Basel, Switzerland. This article is an open access article distributed under the terms and conditions of the Creative Commons Attribution (CC BY) license (<https://creativecommons.org/licenses/by/4.0/>).

1. Introduction

Inverse synthetic aperture radar (ISAR) [1–5] is a microwave sensing technology. Thanks to its advantages such as detecting targets from a distance, at any time of day and in any weather, and so on, it is widely used in national defense and other fields. Through ISAR technology, some information about targets, e.g., size and structure, can be accurately obtained from its reflected echoes, followed by further classification and identification.

For cooperative space targets, their motion is moderate, and thus their attitude remains stabilized during coherent accumulation time. As a result, high-quality ISAR images are generated by using existing imaging methods, e.g., the Range Doppler (RD) algorithm [6,7], thanks to the high signal-to-noise ratio (SNR) echoes with simple Doppler frequency. However, the movement posture of non-cooperative targets is often uncontrollable. Meanwhile, their motion is always accompanied by time-varying characteristics, resulting in complex Doppler frequencies, which make existing ISAR imaging methods more challenging to employ. Furthermore, the resulting ISAR images are usually polluted by noise due to the low SNRs.

To obtain high-quality ISAR images for non-cooperative targets, many methods have recently been developed, and they can be broadly divided into two categories. The former

is the parameter-estimation-based approach. The main principle of this approach is that the echoes in the azimuth dimension are modeled as multi-component polynomial phase signals (MCPPSs) after finishing the range migration correction. Further, the coefficients of the signal are estimated with parameter-estimation-based approaches, such as the high-order ambiguity function (HAF) [8], product high-order matched-phase transform (PHMT) [9], generalized CPF (GCPF) [10], chirp rate–quadratic chirp rate distribution (CRQCRD) [11], product GCPF (PGCPF) [12], integrated parametric cubic phase function (IPC PF) [13], coherent integrated smoothed GCPF (CISGCPF) [14], etc. These methods can obtain high-quality ISAR images for non-cooperative space targets under certain conditions. However, the model mismatch problem of the Doppler signal is inevitable, resulting in defocusing in the azimuth dimension. Meanwhile, the signal of all range bins should be reconstructed, which is time-consuming.

The second method is the time–frequency analysis (TFA)-based imaging approach. The classical methods, e.g., short-time Fourier transform (STFT) [15] and wavelet transform (WT) [16], are applied to ISAR imaging. STFT-based and WT-based imaging approaches are essentially types of linear transformation approaches with no cross-term interference. However, the time–frequency resolution of those methods is low compared with that of the nonlinear transformation methods. Naturally, a TFA based on nonlinear transformation is utilized to image non-cooperative space targets. As a representative of the nonlinear transformation method, the Wigner–Ville distribution (WVD) method [17,18] provides a higher time–frequency resolution. Nevertheless, due to its nonlinear characteristics, the cross-term interference is serious when processing multi-component mixed signals, which deteriorates the ISAR images. To overcome the problem of cross-term interference, the extended WVD approach, e.g., the smoothed pseudo WVD (SPWVD) method [19,20] and the class L polynomial WVD transform (LPWVD) method [21], is introduced to imaging for non-cooperative space targets. However, its performance when suppressing the cross-term interference and the time–frequency resolution should have a trade-off in actuality. In addition, the S-transform (ST) [22] and synchrosqueezing transform (SST)-based [23] ISAR imaging approaches are proposed to suppress the cross-term interference. However, human participation is involved in the process of ISAR imaging. In summary, extended TFA-based methods should be designed for the ISAR imaging of non-cooperative space targets with complex motion.

To generate high-quality ISAR images for non-cooperative space targets with complex motion, this paper proposes an ISAR imaging approach combined high-order synchrosqueezing transform with the modified multi-scale retinex method (HSTMMSR) for non-cooperative space targets. First, to reasonably describe the mobility of a non-cooperative space target, the imaging geometry and signal model for non-cooperative space targets with complex motion are established. Second, the translational motion is compensated using the standard method. Meanwhile, the echoes are modeled as MCPPSs in each range bin. Third, using the HoSST method, the MCPPSs can be transformed into the range–time–Doppler domain, where a coarse ISAR image is obtained with the quality indicator, e.g., image entropy, followed by the MMSR to enhance the result. Finally, several numerical experiments using simulated data and measured data are conducted to demonstrate the validity of the proposed approach.

The rest of this article is organized as follows. In Section 2, the ISAR imaging geometry and signal model for non-cooperative space targets are presented to prepare for the subsequent algorithm development. The proposed method is developed in Section 3, including the ISAR imaging principle of HSTMMSR, the procedure of the proposed algorithm, and some additional considerations. Experimental results and analysis are provided in Section 4 to verify the effectiveness of the proposed method, and some conclusions are summarized in Section 5.

2. Imaging Geometry and Signal Model for Non-Cooperative Space Targets

In this subsection, the ISAR imaging geometry for non-cooperative space targets is presented for the subsequent algorithm development. The standard ISAR imaging geometry model is depicted in Figure 1, where the Cartesian coordinate (X, Y, Z) is established in the target body, the origin O is the rotating center of the targets, and the unit vector of the radar line-of-sight (LOS) and the three-dimensional angular speed of targets are denoted by the vectors \overleftarrow{R} and $\overleftarrow{\Omega}$, respectively. According to the theorem of vector decomposition, the vector $\overleftarrow{\Omega}$ can be divided into components that are parallel to and perpendicular to \overleftarrow{R} , which, respectively, can be represented as $\overleftarrow{\Omega}_e$ and $\overleftarrow{\Omega}_R$. In general, because $\overleftarrow{\Omega}_R$ does not contribute to the imaging, the effective rotating velocity can be denoted as $\overleftarrow{\Omega}_e$.

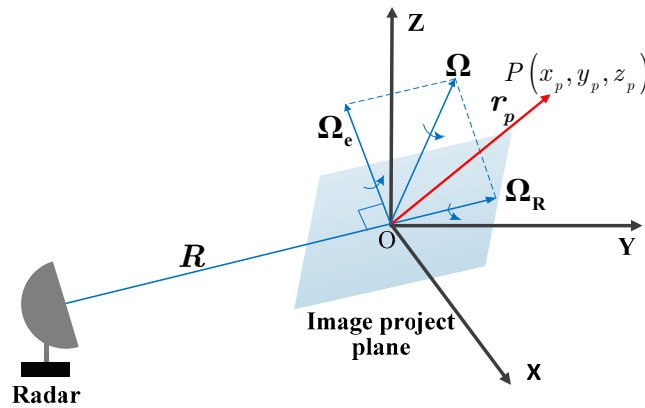


Figure 1. General geometry model for a ship target with complex motion.

Signal Model of Non-Cooperative Targets with Complex Motion

Suppose the space coordinate for the arbitrary scatterer P in the target body is (x_p, y_p, z_p) , \vec{r}_p denotes the rotating radius of the scatterer P , and v_r denotes the translational velocity of the target. Therefore, the Doppler frequency of the scatterer P is

$$f_d = \frac{2}{\lambda} (v_r + (\Omega_e \times r_p) \cdot R), \tag{1}$$

where \times and \cdot , respectively, denote the outer and inner product, and λ denotes the wavelength of the transmitted signal.

As described above, the translational vector v_r and effective rotation vector $\overleftarrow{\Omega}_e$ of the non-cooperative space targets are time-varying during the coherence integration interval. Without loss of generality, in this study, the translational vector v_r and effective rotation vector Ω_e can be modeled as

$$\begin{cases} v_r(t_m) = v_0 + a_0 t_m + \frac{1}{2} r_0 t_m^2 \\ \Omega_e(t_m) = \alpha + \beta t_m + \frac{1}{2} \gamma t_m^2 \end{cases}, \tag{2}$$

where v_0, a_0 , and r_0 denote the radial velocity, acceleration, and acceleration rate, respectively. α, β , and γ represent the coefficients of the constant, first, and second term of Ω_e , respectively, and t_m denotes the slow time. By substituting (2) into (1), we obtain

$$f_d(t_m) = \frac{2}{\lambda} \left\{ \left[(\alpha \times \vec{r}_p) \cdot R + v_0 \right] + \left[(\beta \times \vec{r}_p) \cdot R + a_0 \right] t_m + \left[(\gamma \times \vec{r}_p) \cdot R + r_0 \right] t_m^2 \right\} \tag{3}$$

Based on the relationship between the Doppler frequency and the instantaneous slant range, the instantaneous slant range $R_p(t_m)$ of the scatterer P can be expressed as

$$\begin{aligned}
 R_p(t_m) &= \frac{\lambda}{2} \int_{t_0}^{t_m} f_d dt_m \\
 &= R_p(t_0) + \left[(\alpha \times \vec{r}_p) \cdot \mathbf{R} + v_0 \right] t_m \\
 &\quad + \frac{1}{2} \left[(\beta \times \vec{r}_p) \cdot \mathbf{R} + a_0 \right] t_m^2 \\
 &\quad + \frac{1}{6} \left[(\gamma \times \vec{r}_p) \cdot \mathbf{R} + r_0 \right] t_m^3
 \end{aligned} \tag{4}$$

In this work, suppose that the radar transmits a linear frequency-modulated (LFM) signal, given by

$$s(t_r, t_m) = \text{rect}\left(\frac{t_r}{T_p}\right) \cdot \exp\left\{j2\pi\left(f_c t_r + \frac{1}{2}K_r t_r^2\right)\right\}, \tag{5}$$

where $\text{rect}(x) = \begin{cases} 1, & |x| \leq 1/2 \\ 0, & |x| > 1/2 \end{cases}$, t_r, f_c, K_r , and T_p denote the fast time, carrier frequency, frequency modulation rate, and pulse width, respectively; $t_m = t_r + m \cdot T_p, (m = 0, 1, \dots, M - 1)$ denotes the full time; and M represents the total number of received pulses.

By transmitting the LFM signal, the echoes reflected from the scatterer P satisfy

$$\begin{aligned}
 s(t_r, t_m) &= \sigma_p \cdot \text{rect}\left(\frac{t_r - 2R_p(t_m)/c}{T_p}\right) \cdot \text{rect}\left(\frac{t_m}{T_a}\right) \\
 &\quad \times \exp\left\{j2\pi\left(f_c(t_r - 2R_p(t_m)/c) + \frac{1}{2}K_r(t_r - 2R_p(t_m)/c)^2\right)\right\}
 \end{aligned} \tag{6}$$

where σ_p, c , and T_a denote the reflection coefficient of the scatterer P , the speed of light, and the coherent integration time, respectively.

After baseband demodulation and range compression, the received echoes can be written as

$$\begin{aligned}
 s(t_r, t_m) &= \sigma_p B_r \omega_a(t_m) \text{sinc}\left[B_r\left(t_r - \frac{2R_p(t_m)}{c}\right)\right] \\
 &\quad \times \exp\left[-j\frac{4\pi}{\lambda}R_p(t_m)\right]
 \end{aligned} \tag{7}$$

where B_r denotes the bandwidth of the transmitted signal and $\omega_a(t_m)$ represents the azimuth envelope.

It is worth noting that, from (7), the envelope term $R_p(t_m)$ in SINC [*] causes the range migration, e.g., translational migration and migration, through range cells (MTRCs). It is well-known that the translational motion term in (7) can be compensated for by utilizing standard translational motion compensation algorithms, e.g., envelope correlation [24], global range alignment [25], the image entropy-based method [26], the image contrast-based method [27], and so on. Furthermore, the keystone transform (KT) technique [28] can be adopted to compensate for the MTRCs term. In conclusion, the range migration term can be easily corrected compared with the phase modulation term in (7). It is worth mentioning that the phase modulation term is time-varying due to the time-varying characteristic of non-cooperative targets. Meanwhile, the phase distribution of each scatterer is different on the effect of different rotating centers for different scatterers, invalidating existing ISAR imaging algorithms.

We assume the energies of all scatterers are concentrated into the right range bins after conducting the range migration correction operation. Therefore, the signals in a range bin can be modeled using multi-component quadratic frequency modulation (MCQFM), and the analytical expression of the signal in the l th range cell can be expressed as

$$s_l(t_m) = \sum_{k=1}^K A_k \left\{ \exp\left[j2\pi\left(b_{k,1}t_m + b_{k,2}t_m^2 + b_{k,3}t_m^3\right)\right] + n(t_m) \right\}, \tag{8}$$

where $A_k, b_{k,1} = -2(\alpha \times \vec{r}_p) \cdot \mathbf{R}/\lambda, b_{k,2} = -(\beta \times \vec{r}_p) \cdot \mathbf{R}/\lambda,$ and $b_{k,3} = -(\gamma \times \vec{r}_p) \cdot \mathbf{R}/3\lambda$ represent the amplitude, center frequency, chirp rate, and derivative of the chirp rate, respectively. $n(t_m)$ denotes the additive complex white Gaussian noise with zero mean and variance of 1. As a result, to produce well-focused ISAR images for non-cooperative targets, the time-varying phase term and the additive complex white Gaussian noise in (8) caused by non-cooperative motion need to be precisely compensated for.

3. Proposed Imaging Method

As described above, existing ISAR imaging methods based on TFA are invalid for non-cooperative space targets. There are two possible reasons. The first is that the Doppler frequency of the non-cooperative space targets cannot be described in a uniform way, and the second is that the applicability of the TFA is limited. Therefore, due to the coupling effect of these reasons, obtaining high-quality ISAR images for non-cooperative space targets is challenging. In this section, by considering these issues, we primary focus on the ISAR imaging approach for non-cooperative space targets based on HSTMMSR approaches, which consist of two steps.

3.1. Coarse ISAR Imaging with High-Order Synchrosqueezing Transform

As a high-resolution time–frequency analysis method, HoSST [29,30] is a new extension of the synchrosqueezing transform (SST) method that can extract the instantaneous time-varying frequency of a signal accurately.

Now, we address the signals in the l th range bin, the STFT of which can be expressed as

$$V_f^g(t_m, \eta) = \int s_l(t_m)g^*(\tau - t_m)exp[-j2\pi\eta(\tau - t_m)], \tag{9}$$

where g represents a window function and g^* denotes the complex conjugate of g .

The general STFT-based SST can be defined as

$$T_f^{g,\gamma}(t_m, \eta) = \frac{1}{g^*(0)} \int_{\{\eta, |V_f^g(t_m, \eta)| > \gamma\}} V_f^g(t_m, \eta)\delta(\omega - \omega_f(t_m, \eta)) d\eta, \tag{10}$$

where γ denotes the pre-set threshold, $\delta(\cdot)$ stands for the Dirac distribution, and $\omega_f(t_m, \eta)$ denotes the instantaneous frequency estimated at time t_m and frequency η , defined by

$$\omega_f(t_m, \eta) = R \left\{ \frac{\partial_t V_f^g(t_m, \eta)}{j2\pi V_f^g(t_m, \eta)} \right\} \tag{11}$$

where $R\{x\}$ represents the real-value part of the complex number x and ∂_{t_m} denotes the partial derivative of t_m .

It is noteworthy that, from (9) to (11), the instantaneous frequency of the signal is determined by a low-order term, which is effective to describe space targets with moderate motion. However, for non-cooperative space targets with complex motion, the instantaneous Doppler frequency is intricate; thus, it cannot be accurately presented. Therefore, to precisely extract the complex instantaneous Doppler frequency from the echoes of non-cooperative space targets, the instantaneous Doppler frequency can be modeled as a high-order term.

For high-order SST (HoSST), the instantaneous Doppler frequency is defined using a high-order Taylor expansion for both the amplitude and phase, which means that the Taylor expansion of the signal $s_l(t_m)$ in (8) can be expressed as

$$s_l(t_m) = exp \left\{ \sum_{k=0}^N \frac{[\log(A)]^{(k)}(t_m) + j2\pi\phi^{(k)}(t)}{k!} (\tau - t_m)^k \right\} \tag{12}$$

where $[Z]^{(k)}(t_m)$ represents the k th derivative in terms of Z at time t_m . Therefore, (10) can be rewritten as

$$\begin{aligned}
 V_f^g(t_m, \eta) &= \int s_l(\tau + t_m)g^*(\tau) \exp[-j2\pi\eta t_m]d\tau \\
 &= \int \exp\left\{ \sum_{k=0}^N \frac{[\log(A)]^{(k)}(t_m) + j2\pi\phi^{(k)}(t_m)}{k!} (t)^k \right\} \times g^*(\tau)\exp(-j2\pi\eta t_m)d\tau
 \end{aligned}
 \tag{13}$$

According to (13), the local instantaneous frequency $\omega_f(t_m, \eta)$ can be rewritten as

$$\begin{aligned}
 \omega_f(t_m, \eta) &= \frac{[\log(A)]'(t_m)}{j2\pi} + \phi'(t_m) \\
 &+ \sum_{k=2}^N \frac{[\log(A)]^{(k)}(t_m) + j2\pi\phi^{(k)}(t_m)}{j2\pi(k-1)!} \cdot \frac{V_f^{g^{k-1}}(t_m, \eta)}{V_f^g(t_m, \eta)}
 \end{aligned}
 \tag{14}$$

The frequency modulation operator $q_{\eta, f}^{[k, N]}$ can be defined as

$$q_{\eta, f}^{[k, N]} = \frac{[\log(A)]^{(k)}(t_m) + j2\pi\phi^{(k)}(t_m)}{j2\pi(k-1)!}
 \tag{15}$$

In addition, the N th-order local complex instantaneous frequency $\omega_{\eta, f}^{[N]}$ at time t_m and frequency η can be given by

$$\omega_{\eta, f}^{[N]}(t_m, \eta) = \begin{cases} \omega_f(t_m, \eta) + \sum_{k=2}^N q_{\eta, f}^{[k, N]}(t_m, \eta)(-x_{k,1}(t_m, \eta)) \\ V_f^g(t_m, \eta) \neq 0, & x_{j, j-1}(t_m, \eta) \neq 0 (j \geq 2) \\ \omega_f(t_m, \eta) & \text{otherwise} \end{cases}
 \tag{16}$$

As a result, the $\omega_f(t_m, \eta)$ can be replaced by $\omega_{\eta, f}^{[N]}(t_m, \eta)$ in (10), given by

$$T_{N, f}^{g, \gamma}(t_m, \omega) = \frac{1}{g^*(0)} \int_{\{\eta, |V_f^g(t_m, \eta)| > \gamma\}} V_f^g(t_m, \eta) \delta(\omega - \omega_{\eta, f}^{[N]}(t_m, \eta)) d\eta
 \tag{17}$$

Additionally, the signal with complex instantaneous frequency can be reconstructed, given by

$$s_l(t_m) = \int_{\{\omega, |\omega - \phi(t_m)| < d\}} T_{N, f}^{g, \gamma}(t_m, \omega) d\omega
 \tag{18}$$

Therefore, compared with the conventional STFT method, the instantaneous frequency with HoSST is more appropriate for non-cooperative space targets because the local instantaneous frequency is modeled as a high-order polynomial, which is consistent with the nature of highly complex motion. As a consequence, the high-resolution two-dimensional time–frequency analysis result can be obtained. Inspired by the high-resolution time–frequency characteristic of HoSST, in this work, a coarse ISAR image can be produced using the HoSST-based time–frequency analysis method.

Using HoSST to process the signals in each range bin, the range–time–Doppler matrix is obtained, where different frequencies correspond to different ISAR images. Therefore, the entropy is adopted as an image quality indicator to extract the optimal ISAR images, given by

$$I(x, y) = \operatorname{argmax}_{w_f} \left\{ I(t_r, w_f, t_r) \right\}
 \tag{19}$$

where $\max_{w_f}\{\cdot\}$ represents the maximum value in terms of the Doppler frequency w_f , $I(x, y)$ denotes the optimal ISAR images, and (x, y) denotes the pixel coordinate.

3.2. Fine ISAR Imaging with Modified Multi-Scale Retinex

It is well known that the electromagnetic scattering characteristic of targets determines whether the ISAR images are accompanied by significant sparse features, resulting in large scattering intensity differences and low visualization of weak component in the ISAR images, which is not conducive for the interpretation of the images or for the analysis of the morphological structure of the targets. Furthermore, due to the highly complex motion characteristic of non-cooperative targets, the SNR of the echoes is low and the ISAR images are polluted by noise. To overcome the obstacle above, in this study, the modified multi-scale retinex (MMSR) method is adopted to conduct the enhancement operation for the ISAR images of non-cooperative space targets.

Based on the retinex theory, the arbitrary pixel value $I(x, y)$ of ISAR images can be obtained using the following expression:

$$I(x, y) = L(x, y) * R(x, y) \quad (20)$$

where $L(x, y)$ denotes the illuminated intensity component and $R(x, y)$ represents the reflected component.

In reality, the single-scale retinex (SSR) method is utilized to enhance the ISAR images. However, trade-offs need to be made between detail enhancement and contrast enhancement, among other factors, which increases the difficulty of the operations. Inspired by the advantage of the multiple-scale parameter for SSR, the MMSR is utilized to complete the above tasks, given by

$$I_{MMSR}(x, y) = \gamma^{R_{MMSR}(x, y)}, \quad (21)$$

where γ denotes the base of the logarithm, which is related to the log in (22) and $R_{MMSR}(x, y)$ represents the enhancement factor of the ISAR images, given by

$$R_{MMSR}(x, y) = \sum_{n=1}^N \omega_n \{ \log[I(x, y)] - \log[I(x, y) \oplus G_n(x, y)] \}, \quad (22)$$

where ω_n and G_n , respectively, denote the weighting coefficient of the n -th scale parameter and the Gaussian distribution function, given by

$$G_n(x, y) = K_n \cdot \exp\left(\frac{-(x^2 + y^2)}{2\sigma_n^2}\right), \quad (23)$$

where σ_n^2 denotes the scale parameter, N denotes the number of the scale parameter, and K_n denotes the normalization factor, given by

$$\iint G_n(x, y) dx dy = 1 \quad (24)$$

3.3. ISAR Imaging of the Proposed Method

Based on the excellent time–frequency analysis performance, a novelty ISAR imaging approach that combines HOSST with MMSR is proposed for non-cooperative space targets with complex motion. The detailed implementation process is summarized below.

Conduct range compression operation for raw echoes;

1. Perform range migration compensation with existing methods to concentrate the energies into the same range cells;

Initialize iteration i as 1 and complete the time–frequency analysis operation using the HOSST approach along the azimuth dimension;

Let $i = i + 1$ and repeat the complete time–frequency analysis based on HOSST until $i = N$, where N denotes the number of range cells;

Rearrange the time series and extract the coarse ISAR image based on the image indicator, e.g., image entropy or image contrast;

Enhance the coarse ISAR images by using the MMSR;

2. Output the fine ISAR images of non-cooperative space targets.

To summarize, the flowchart of the entire ISAR imaging approach is presented in Figure 2.

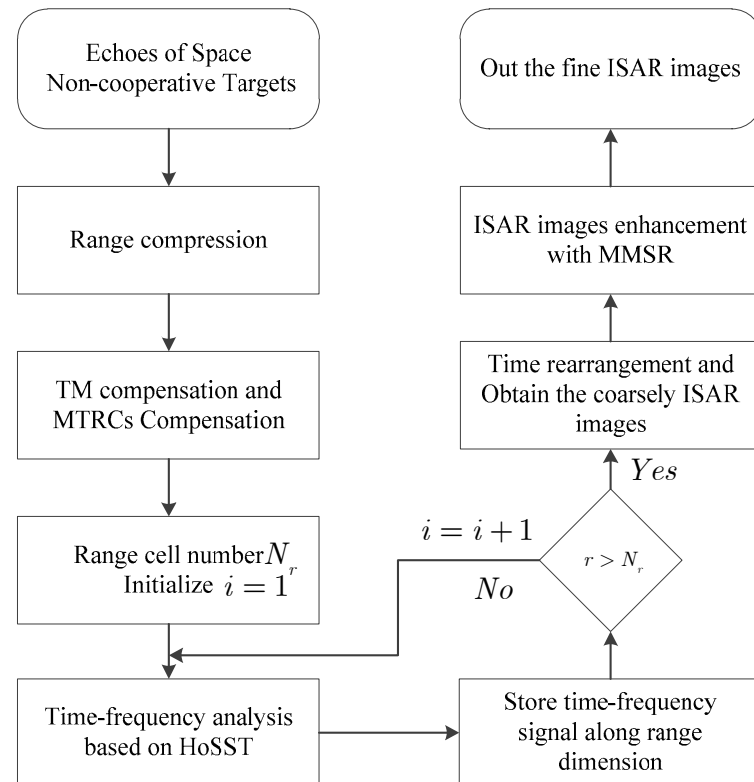


Figure 2. Flowchart of the proposed method.

3.4. Some Considerations for the Application

3.4.1. Numerical Analysis and Performance Comparison

To further illustrate the effectiveness of the proposed method, MCS including chirp frequency modulation, polynomial phase frequency modulation, and sinusoidal frequency modulation was processed using WVD, STFT, SST, and HoSST.

The time–frequency analysis results using simulated data with 1024 samples are presented in Figure 3; the time-domain characteristic of the MCS is shown in Figure 3a. It can be seen that the MCS is chaotic. It is clear from Figure 3b that the MCS is composed of three signals with different frequencies. The time–frequency result of WVD for MCS is shown in Figure 3c. It is noteworthy that the clustering characteristic is poor, which seriously affects the ISAR imaging performance for non-cooperative space targets. It is worth noting that, as seen in Figure 3d, the time–frequency result of STFT has no cross-term interference. Nevertheless, the time–frequency resolution is low. The time–frequency result of SST is presented in Figure 3e. It should be noted that its time–frequency resolution is higher than those of WVD and STFT. Meanwhile, cross-terms interference is absent. However, the time–frequency resolution of the sinusoidal frequency modulation signal is limited. In contrast, the high-quality time–frequency signal is reconstructed using the HoSST, as shown in Figure 3f. In addition, thanks to the robustness and focusing performance, the signals reconstructed from Figure 3a are consistent with the instantaneous frequency distribution of Figure 3b. As a result, compared with WVD, STFT, and SST, the HoSST has an outstanding time–frequency focusing characteristic, providing a novel method for the design of ISAR imaging algorithms.

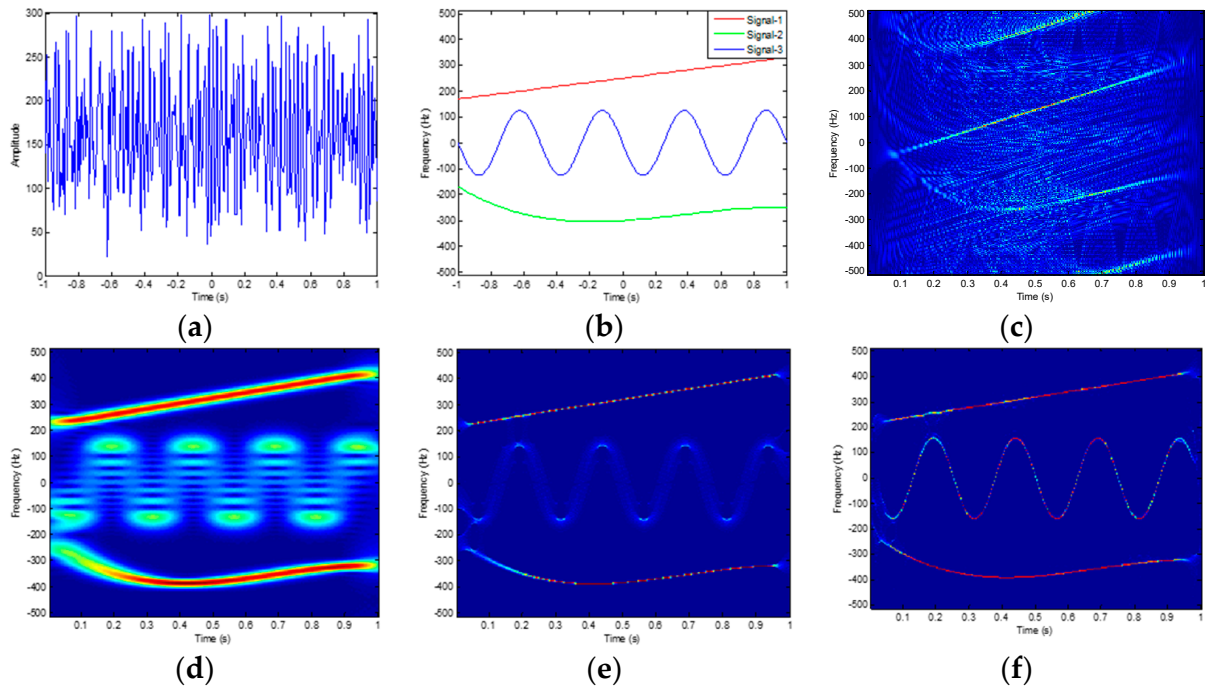


Figure 3. Time–frequency diagram of mixed signals. (a) Time domain characteristics of mixed signals. (b) Instantaneous frequency characteristics of mixed signals. (c) WVD method. (d) STFT method. (e) SST method. (f) HoSST method.

3.4.2. Computational Complexity Analysis

In this subsection, the computational complexities of RD, WVD, STFT, SST, and the proposed method are theoretically analyzed. Generally, some procedures with low computational complexity in the algorithm implementation process are not included in calculating the computational complexity. Furthermore, $N \log_2(N)$ floating-point operations (FLOPs) are required in order to conduct the operation of Fourier transform (FT) or inverse Fourier transform (IFT) for N -point data, and N FLOPs are required to execute one-time complex multiplications for N -point data. Now, suppose the size of the echoes in this work is $N_a \times N_r$.

In general, the procedure of RD consists of a range compression procedure and an azimuth compression step with two-time FFT operations, one-time multiplication, and one-time IFFT. Thus, the computational complexity is

$$C_{RD} = O \left\{ \begin{matrix} 2N_a N_r \log_2(N_r) + \\ N_a N_r + N_a N_r \log_2(N_a) \end{matrix} \right\} \quad (25)$$

The procedure of the WVD method is composed of range compression and time–frequency analysis in the azimuth dimension. The computational complexity of the range compression is $O(2N_a N_r \log_2(N_r) + N_a N_r)$, and the computational cost for N_a -point data during the time–frequency analysis of the WVD method is $O(4N_a^3 + N_a^2 \log_2(N_a))$. Hence, the computational complexity of the WVD approach is

$$C_{WVD} = O \left\{ \begin{matrix} 2N_a N_r \log_2(N_r) + N_a N_r \\ + N_r (N_a N_r \log_2(N_a)) \end{matrix} \right\} \quad (26)$$

Based on the analysis mentioned in Ref. [18], after the range compress operation, the echoes are iteratively time–frequency analyzed in each range bin using the STFT method along azimuth dimension. Meanwhile, the length of the processing core for STFT is $N_a/4$. The computational complexity with STFT processing for N_a -point data is

$N_a(N_a/8 + N_a \log_2(N_a))$. Therefore, the computational complexity using the STFT method for $N_a N_r$ echoes is

$$C_{STFT} = O \left\{ \begin{array}{l} 2N_a N_r \log_2(N_r) + N_a N_r \\ + N_r N_a (N_a/8 + N_a \log_2(N_a)) \end{array} \right\} \quad (27)$$

For the SST method, based on the analysis in Ref. [23], a Gaussian window function is adopted, the implementation procedure of which consists of three steps, namely, the parameters calculation, SST processing for the time–frequency signal, and the signal component extraction. The total computational cost for the corresponding parameters calculation, SST processing for the time–frequency signal, and the signal component extraction is $N_a N_r (3N_a \log_2(N_a) + N_a)$. Therefore, the computational cost of the SST method for $N_a N_r$ echoes is

$$C_{SST} = O \left\{ \begin{array}{l} 2N_a N_r \log_2(N_r) + N_a N_r \\ + N_a N_r (3N_a \log_2(N_a) + N_a) \end{array} \right\} \quad (28)$$

In this work, the implementation procedure of the proposed method is the corresponding parameters calculation, the estimations of the frequency modulation, the reassignment step, and image enhancement. The total computational cost of the corresponding parameters calculation, the estimations of the frequency modulation, and the reassignment step for N_a data is $N_a (14N_a \log_2(N_a) + 10N_a)$. The cost of image enhancement is determined by the size of the ISAR images. Suppose the size of this work is MN ; thus, the cost is MN . Therefore, the total computational complexity of the proposed method for $N_a N_r$ echoes is

$$C_{Proposed} = O \left\{ \begin{array}{l} 2N_a N_r \log_2(N_r) + N_a N_r \\ + N_a N_r (N_a \log_2(N_a) + N_a) + MN \end{array} \right\} \quad (29)$$

In conclusion, based on the analysis mentioned above, all methods have a range compression operation; thus, the comparison for the computational cost of those methods is determined by the time consumption in the azimuthal dimensional. The computational cost of the RD method is the lowest of those five methods. Compared with the time–frequency analysis method for WVD and STFT, the computational complexity of the proposed approach is a burden because the high-order local instantaneous frequency modulation should be obtained, which is consistent with the analysis mentioned in Section 3.1. Furthermore, the computational complexity of SST is higher than that of the proposed method.

4. Experimental Results and Analysis

In this section, the simulated and measured data are adopted to verify the validity of the proposed method. Meanwhile, some typical time–frequency analysis methods including RD, WVD, STFT, and SST are performed for comparison.

4.1. ISAR Imaging with Simulated Experiments

In this subsection, the simulated data are generated using the radar system parameters and motion parameters presented in Table 1, and the structure of a non-cooperative space target composed of 42 scatterers is presented in Figure 4.

Table 1. Radar system and target motion parameters.

Parameter Name	Value
Carrier frequency	10 GHz
Transmit bandwidth	200 MHz
Pulse repetition	300 Hz
Range sample frequency	300 MHz
Effective echo pluses	256
Rotational angular velocity	0.022 rad/s
Rotational angular acceleration	0.012 rad/s ²
Rotational angular acceleration rate	0.015 rad/s ³

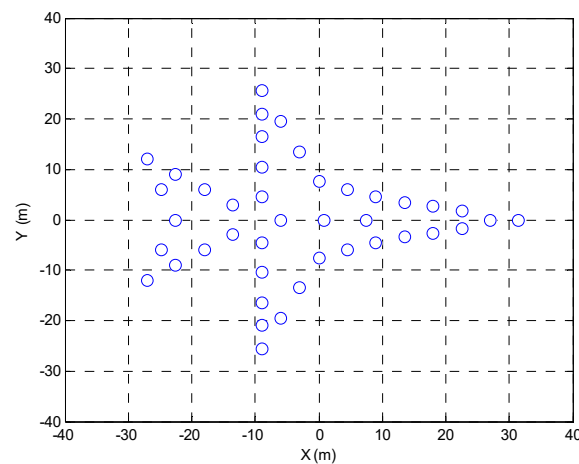


Figure 4. Space target scatter model of ISAR imaging.

To verify the anti-noise performance of those methods, white Gaussian noise is added to the echoes (after range compression), and the analytic expression of SNR can be defined as

$$SNR = 10\log_{10}\left(\frac{\text{Mean Power of Signal}}{\text{Power of Noise}}\right) \tag{30}$$

The ISAR imaging results of the RD method [5], the WVD method [15], the STFT method [18], the SST method [23], and the proposed method under SNRs of 5 dB and −5 dB, respectively, are presented in Figures 5–9. As seen in Figure 5a, due to the non-cooperative characteristics, the ISAR image obtained with the RD method is seriously defocused in the azimuth dimension. The ISAR imaging results using the WVD method are provided in Figure 6. Due to the influence of cross-term interference, the structure of the airplane is hard to observe, especially under the −5 dB condition. The ISAR imaging results obtained with STFT are provided in Figure 7. The results are seriously defocused under the SNR = 5 dB and SNR = −5 dB conditions. The ISAR imaging results using SST and the proposed method are presented in Figures 8 and 9, respectively. It is clear that the proposed method obtains a well-focused and clear target image. In addition, it should be pointed out that, from Figures 5–9, compared with the other four methods, the proposed approach presents a better anti-noise performance, shown in Figures 5b, 6b, 7b, 8b and 9b. Therefore, the proposed approach has advantages in ISAR imaging performance for non-cooperative space targets.

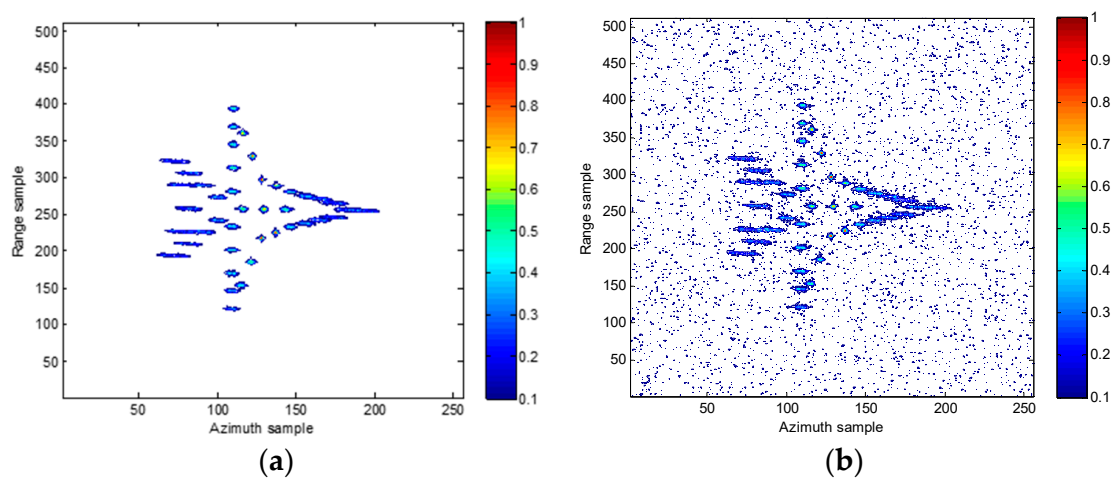


Figure 5. RD-method ISAR imaging results: (a) SNR = 5 dB; (b) SNR = −5 dB.

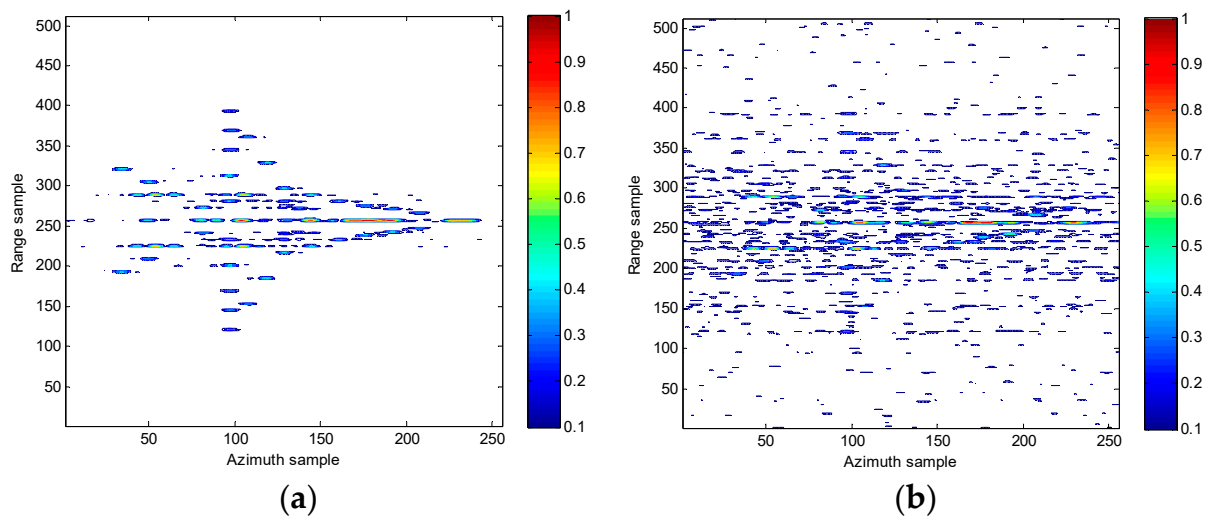


Figure 6. WVD-method ISAR imaging results: (a) SNR = 5 dB; (b) SNR = -5 dB.

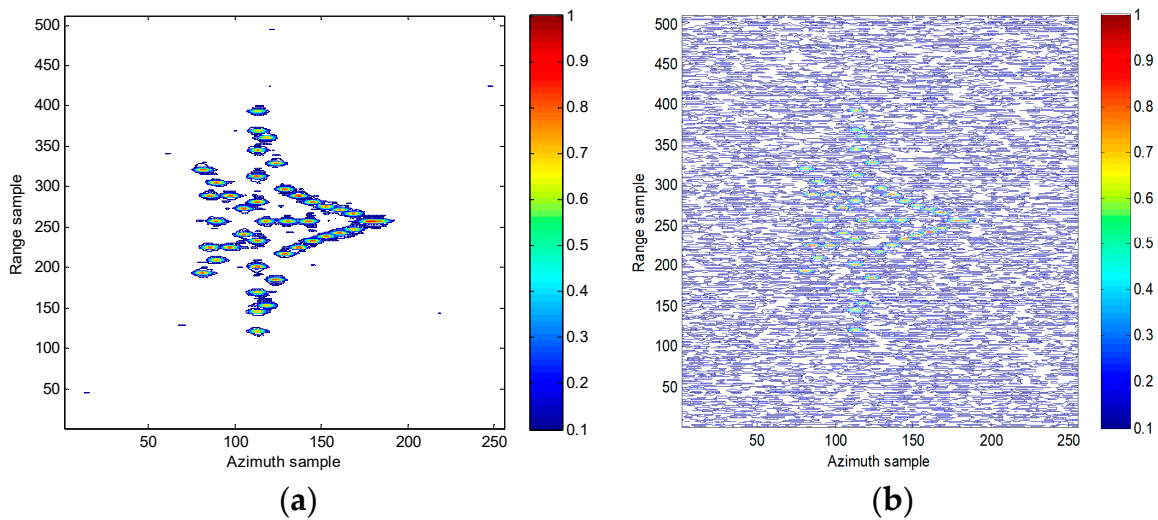


Figure 7. STFT-method ISAR imaging results: (a) SNR = 5 dB; (b) SNR = -5 dB.

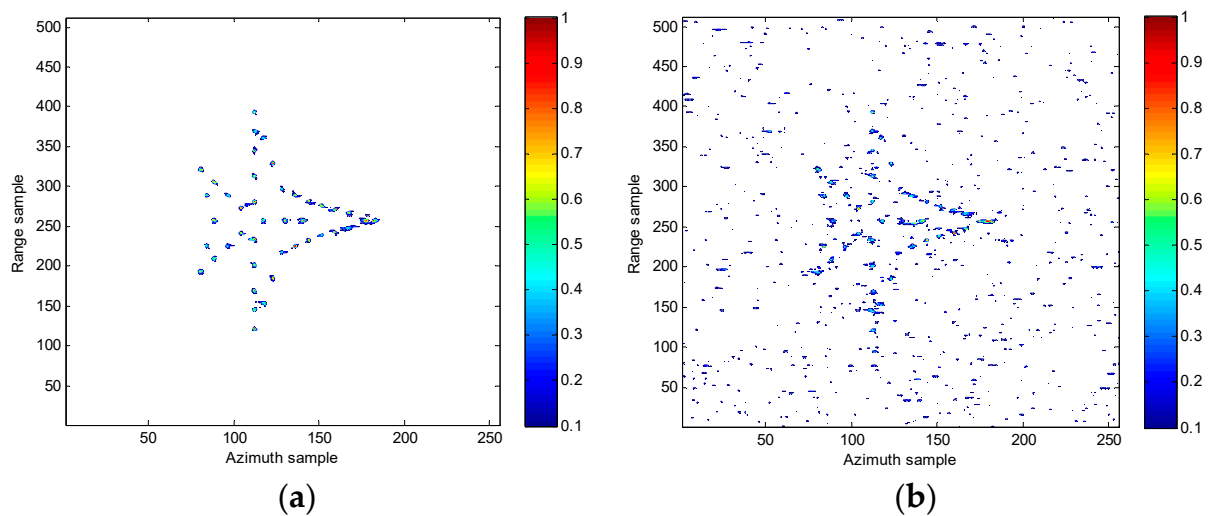


Figure 8. SST-method ISAR imaging results: (a) SNR = 5 dB; (b) SNR = -5 dB.

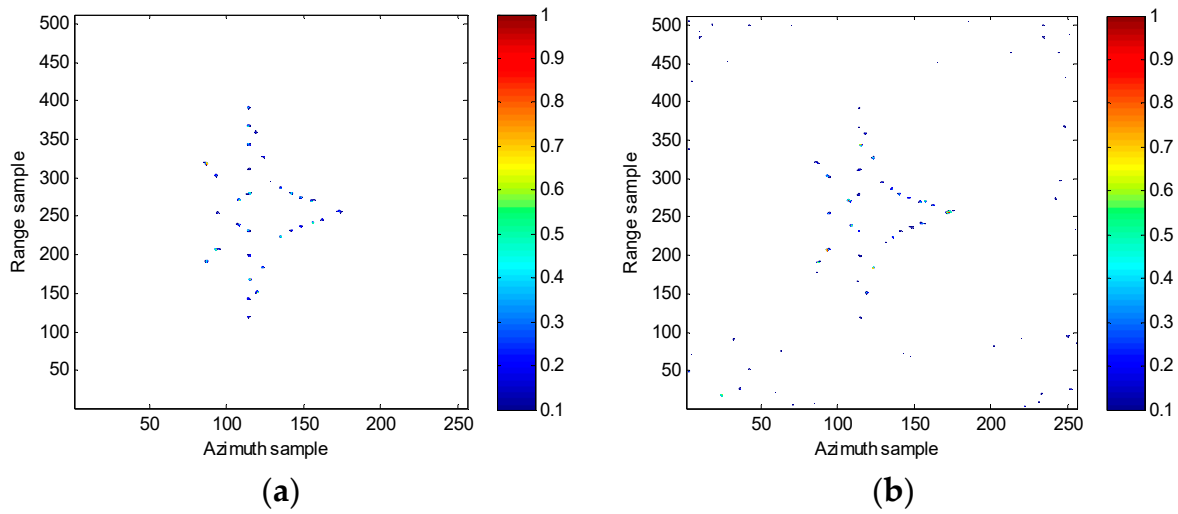


Figure 9. The ISAR imaging results obtained using the proposed method: (a) SNR = 5 dB; (b) SNR = −5 dB.

In addition to the quantitative analysis of the ISAR imaging performance of the different approaches, the image entropy IE [31,32] and image contrast IC [33–35] were adopted as criteria to evaluate the images’ quality, and they are, respectively, defined below. First:

$$IE = \sum_{m=0}^{M-1} \sum_{n=0}^{N-1} \frac{|g(m,n)|^2}{S} \ln \frac{S}{|g(m,n)|^2}, \tag{31}$$

where $S = \sum_{m=0}^{M-1} \sum_{n=0}^{N-1} |g(m,n)|^2$; m represents the number of azimuth pulses; and n denotes the number of range cells. Second:

$$IC = \frac{\sqrt{E\{[g^2(m,n) - E(g^2(m,n))]^2\}}}{E\{g^2(m,n)\}} \tag{32}$$

where $E\{\cdot\}$ denotes the expectation operator.

The image entropy and image contrast of each ISAR imaging results, obtained using the RD, STFT, WVD, and SST methods and the proposed method with different SNRs, are provided in Figure 10, where the 100-time Monte Carlo experiments conducted are shown. According to the curve of the image entropy and contrast, the proposed method has a better imaging performance than that of the other methods. Moreover, with the decrease in SNR, the advantage of the proposed method becomes more obvious, illustrating the anti-noise performance of the proposed method.

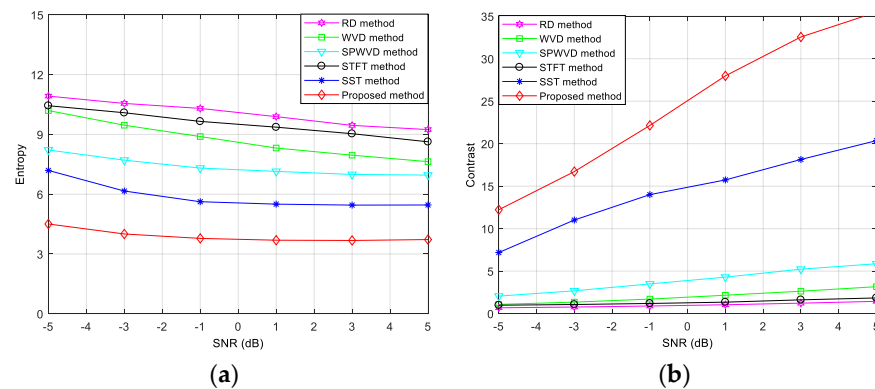


Figure 10. Performance comparison. (a) Image entropy results of different imaging methods versus SNR. (b) Image contrast of different imaging methods versus SNR.

The ISAR imaging cost of the different approaches is provided in Figure 11. The running time of the RD method is the lowest for all the different SNRs, followed by the WVD method and the STFT method. In addition, compared with the SPWVD method and the SST method, the proposed method takes less time, which is consistent with the theory analysis mentioned above. Therefore, by accepting a trade-off between computational complexity and ISAR imaging performance, the proposed method is a promising imaging method for non-cooperative space targets.

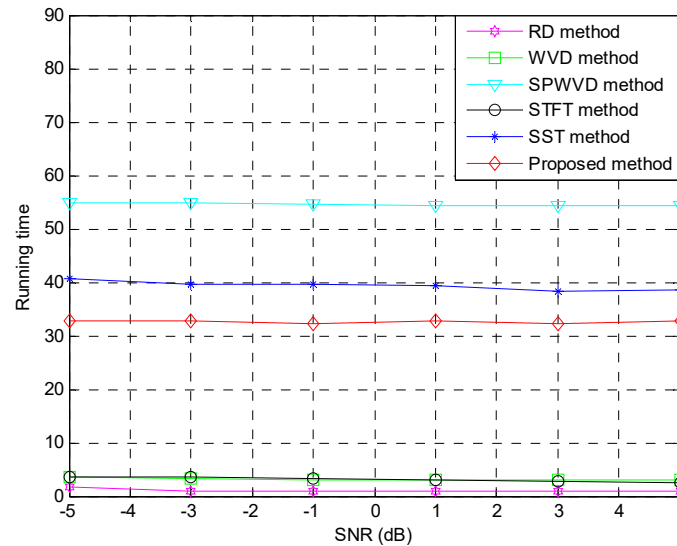


Figure 11. Computational complexity of different methods against SNR.

4.2. ISAR Imaging under Different Motion Parameters

In this subsection, to verify the validity of the studied methods under different motion conditions, three motion parameters are presented (Table 2), where the model is as shown in Figure 4 and the SNR, added in echoes (after range compression), is -3 dB. The ISAR imaging results of the different methods are provided in Figure 12. It is noteworthy that, as seen in Figure 12, the defocusing of the imaging results with the RD method is clear under different motion parameters, shown in Case One, Case Two and Case Three in Figure 12a,b. In addition, the structure of the airplane is submerged in the interference of the noise. Furthermore, the defocusing of the imaging results using the STFT method and the SST method is also serious, shown in Case one, Case Two and Case Three in Figure 12c,d. Moreover, to quantitatively analyze the imaging results, the entropy and contrast under three cases for the different imaging approaches are determined, provided in Table 3. It is worth noting that, as seen in Table 3, the entropy and contrast for the imaging results of the proposed method are the best compared with those of the RD, WVD, STFT, and SST methods, which indicates the effectiveness of the imaging performance of the proposed method. Therefore, on this basis, we can draw the conclusion that the proposed approach has robustness for non-cooperative space targets under different motion parameters.

Table 2. Different motion parameters against the three cases.

Case	Velocity	Rotational Angular Velocity (rad/s)	Rotational Angular Acceleration (rad/s ²)	Rotational Angular Acceleration Rate (rad/s ³)
Case One		0.05	0.05	0.015
Case Two		0.04	0.02	0.01
Case Three		0.04	0.05	0.01

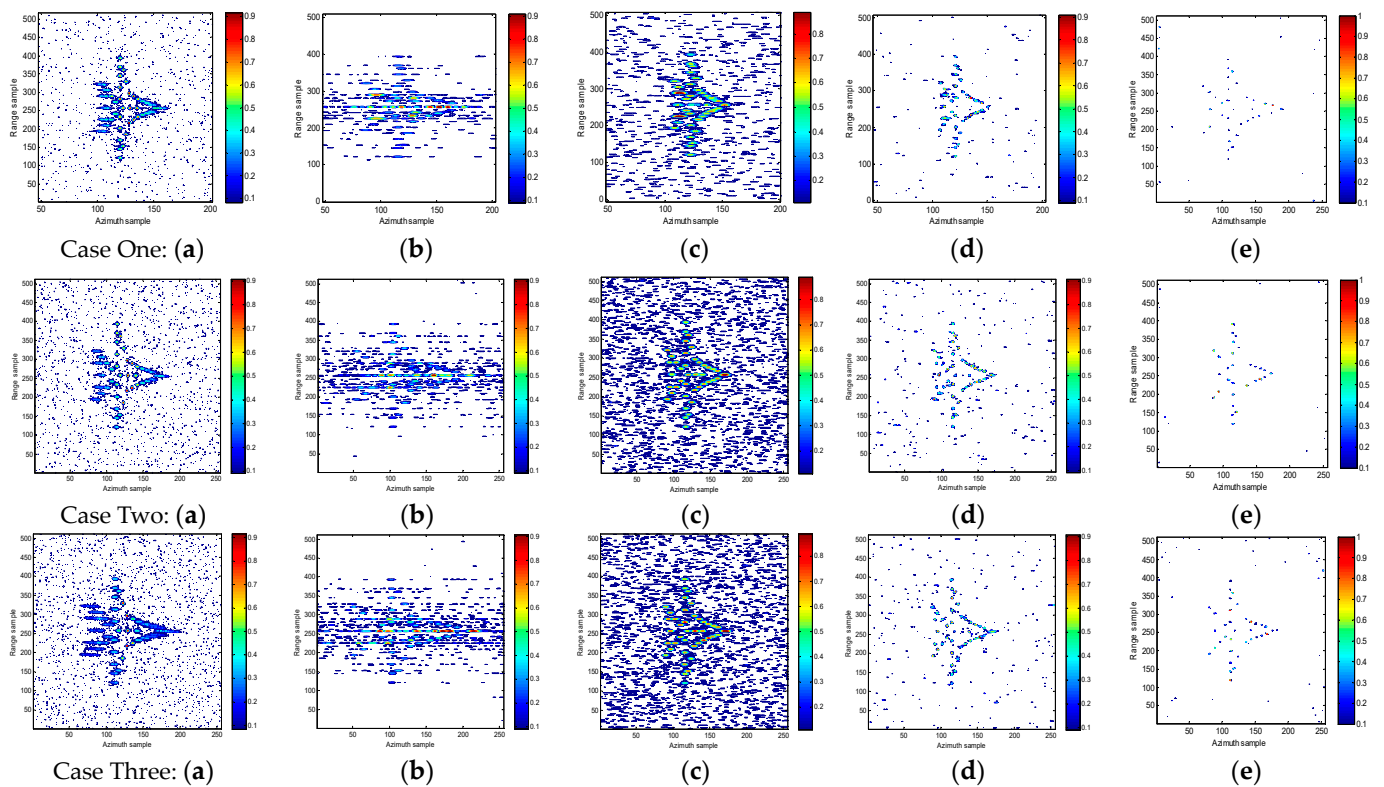


Figure 12. ISAR imaging results with the RD, WVD, STFT, and SST methods and the proposed method in the three cases.

Table 3. Entropy and contrast in the three cases.

Method	Case One		Case Two		Case Three	
	Entropy	Contrast	Entropy	Contrast	Entropy	Contrast
RD	10.634	0.758	10.704	0.742	10.87	0.745
WVD	9.474	1.352	9.612	1.327	9.458	1.376
STFT	10.657	0.777	10.677	0.776	10.671	0.776
SST	6.053	12.532	6.12	12.186	6.095	12.378
Proposed method	4.197	16.362	3.897	17.317	3.91	16.68

4.3. ISAR Imaging under Inhomogeneous Condition

In this subsection, we describe the experiment conducted on the rotation of the targets, which was not completed, but rather limited to a given variable angle. Considering that the rotation is related to the rotational angular velocity (RAV), rotational angular acceleration (RAA), and rotational angular acceleration rate (RAR), the RAV, RAA, and RAR for this experiment are provided in Figure 13, where the values vary randomly within a certain range. The horizontal axis denotes the coherence processing time, and the vertical coordinates represent the corresponding values.

In addition, the imaging results from using the RD, WVD, STFT, and SST methods and the proposed method are presented in Figure 14, where -3 dB white Gaussian noise is added into the echoes. It is noteworthy that the imaging performance of the proposed method is superior to that of the conventional imaging approach, shown in Figure 2a–e. Furthermore, the entropy and contrast are introduced in Table 1 to quantitatively analyze the imaging results. It is worth pointing out that, as seen in Table 4, compared with the

other methods, the entropy of the imaging result from the proposed method is the smallest and the contrast of the imaging results from the proposed method is maximal.

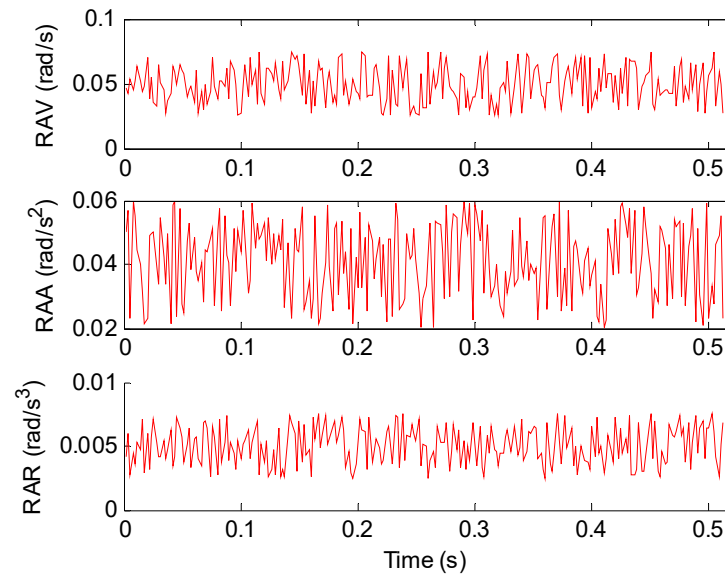


Figure 13. RAV, RAA, and RAR under different coherence processing intervals.

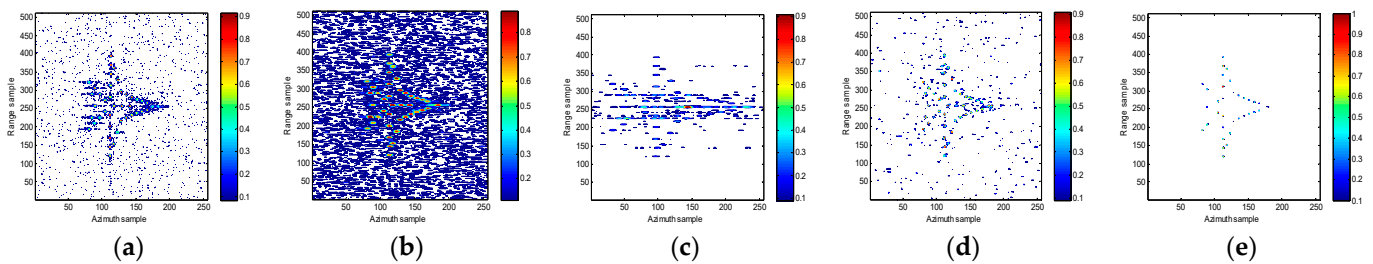


Figure 14. Imaging results of different methods against velocity. (a) RD method. (b) WVD method. (c) STFT method. (d) SST method. (e) Proposed method.

Table 4. Entropy and contrast of the different results.

Method	Entropy	Contrast
RD method	10.4461	0.7979
WVD method	9.4833	1.3691
STFT method	10.7457	0.7540
SST method	6.1907	11.7239
Proposed method	4.283	15.890

4.4. ISAR Imaging under Shadowing Condition

To further verify the imaging performance under a shadowing condition, in this subsection, the tail of targets is shielded from 0.26 s to 0.32 s, and the wing of targets is shielded from 0.42 s to 0.48 s. The method is shown in Figure 15, where 0 and 1, respectively, represent shadowing and not shadowing.

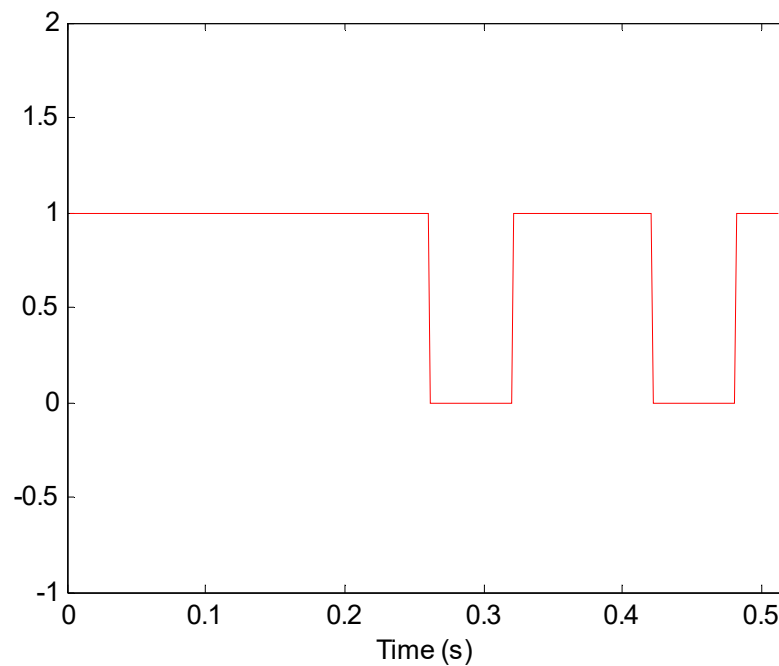


Figure 15. Shadowing and not shadowing time.

The imaging results are provided in Figure 16. In addition, -3 dB white Gaussian noise was added into the echoes. It is worth noting that the proposed method can clearly reconstruct the outline of the targets, as shown in Figure 16. Meanwhile, the imaging performance of the proposed method is superior to that of the other methods. In addition, the entropy and contrast of each method are presented in Table 5; it is clear that the entropy of the imaging result from the proposed method is the smallest, and the contrast of the imaging results from the proposed method is maximal, proving that the proposed approach is a good candidate in the context of missing data.

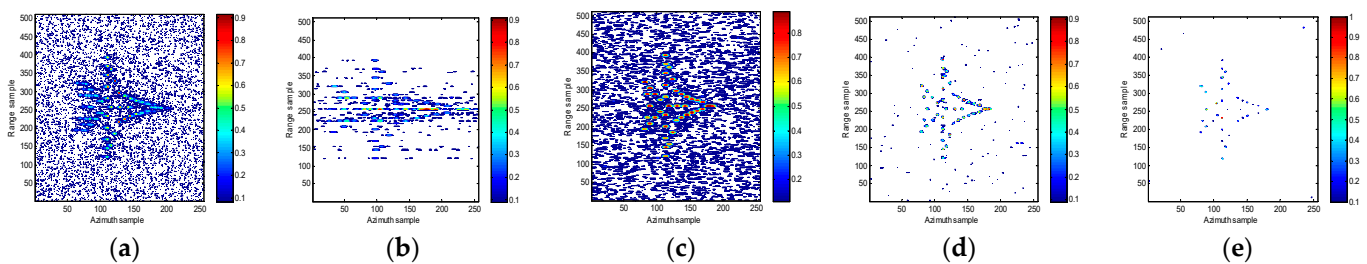


Figure 16. Imaging results of different methods under shadowing condition. (a) RD method. (b) WVD method. (c) STFT method. (d) SST method. (e) Proposed method.

Table 5. The entropy and contrast of different methods.

Method	Entropy	Contrast
RD method	10.6857	0.7644
WVD method	9.1565	1.5103
STFT method	10.5491	0.8204
SST method	5.8319	14.5779
HOSST method	4.1358	16.378

4.5. ISAR Imaging with Measured Data

In this subsection, the real data of a Boeing B727 airplane provided by the U.S. Naval Research Laboratory [36,37] are utilized to verify the validity of the proposed method. The range samples, azimuth samples, carrier, and bandwidth, respectively, are 64, 256, and 9 GHz, and 150 MHz. Now, suppose the range migration has been ideally corrected. The imaging result from the RD method is shown in Figure 17a, in which the image is seriously defocused in the azimuth dimension. The imaging result from WVD is shown in Figure 17b. It is clear that the ISAR image is smeared severely due to the impact of cross-terms and false values, providing less information for the structure of the non-cooperative space target. The ISAR imaging results based on SPWVD are presented in Figure 17c. Here, some weak scatterers disappear, especially the wing and the tail of the airplane. Therefore, it is difficult to reconstruct the structure of the non-cooperative space accurately. The ISAR imaging results based on the STFT method have low resolution, as shown in Figure 17d. Furthermore, in addition to the loss of some structural information, e.g., the wing information, the SST method can basically reconstruct the attitude of the targets, as presented in Figure 17e. Finally, the ISAR imaging results of the proposed method are shown in Figure 17f, where the structure of the target is clear compared with those in the RD, WVD, SPWVD, STFT, and SST results. To further quantitatively analyze the imaging quality, the image entropy, contrast, and imaging time are listed in Table 6, respectively, where it is clear that the entropy of the ISAR images with the proposed method is relatively smaller and its contrast is relatively larger, indicating that the proposed approach may be more suitable for non-cooperative space target imaging. In addition, taking the trade-off between imaging performance and computational complexity into consideration, the proposed approach can be characterized as a more attractive candidate for non-cooperative space ISAR imaging in real applications.

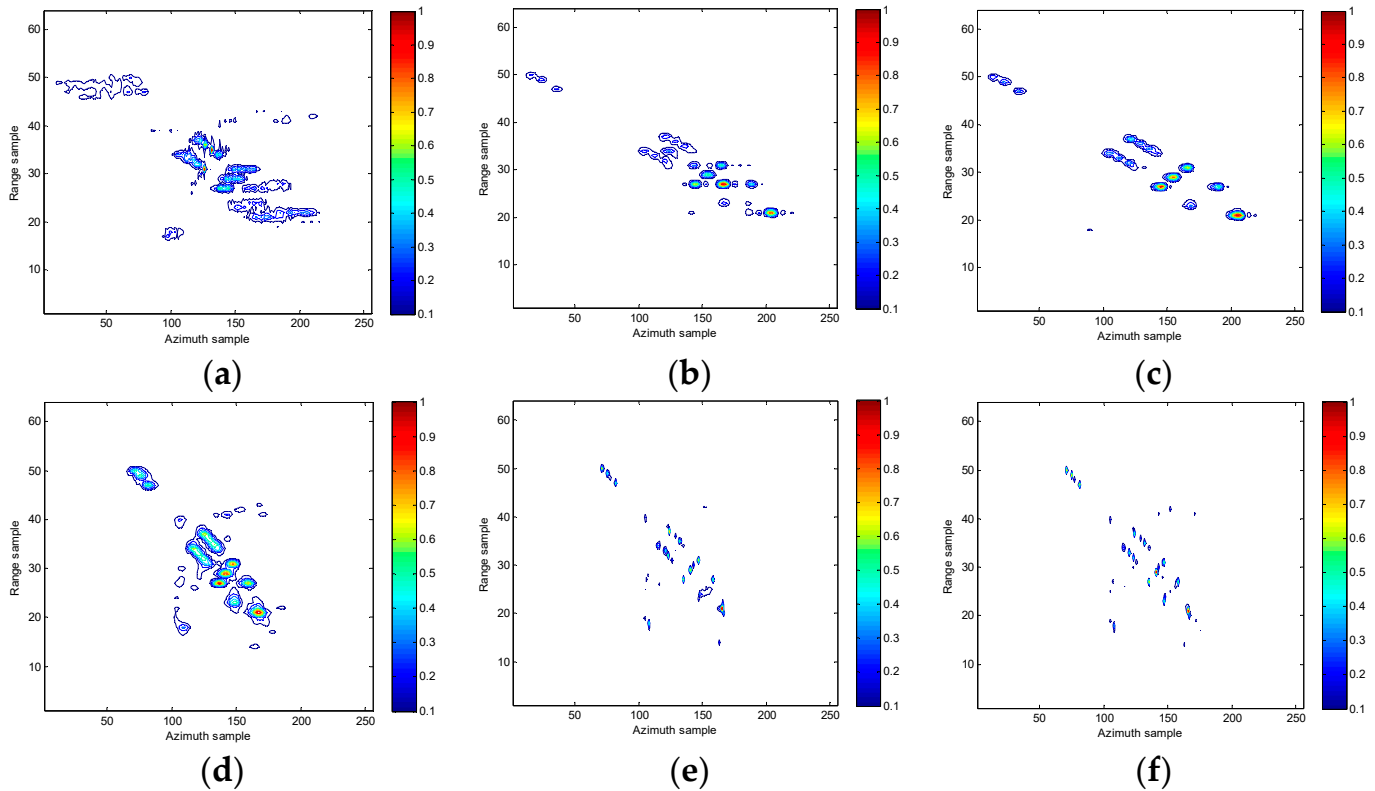


Figure 17. The image results of B727. (a) ISAR image based on RD. (b) ISAR image based on WVD. (c) ISAR image based on SPWVD. (d) ISAR image based on STFT. (e) ISAR image based on SST. (f) ISAR image based on HOSST.

Table 6. Image entropy and contrast of different methods.

Method	Entropy	Contrast	Time(s)
RD method	6.6428	2.3968	0.668
WVD method	5.2811	4.4691	0.764
SPWVD method	4.9003	6.8133	6.822
STFT method	5.8855	3.6353	0.716
SST method	3.8223	10.5464	4.541
Proposed method	3.4621	11.7636	4.045

5. Discussion

ISAR technology is a vital method for remote sensing thanks to its all-day, all-weather, and remote sensing abilities, and so on, which mean that it can obtain the two-dimensional or three-dimensional structures of targets, resulting in improved recognition and classification performance.

For cooperative targets with moderate motion, their Doppler frequencies are simple, so they can be estimated with conventional approaches, followed by high-resolution ISAR images. However, for non-cooperative targets with complex motion, their motion is accompanied by the characteristic of time-varying, e.g., an airplane with three-dimensional rotational motion. Therefore, the Doppler frequencies cannot be described and fitted with traditional linear characteristics, especially under low-SNR conditions, resulting in defocusing.

To obtain high-resolution ISAR images for non-cooperative targets under low-SNR conditions, the recovery of the corresponding time-varying Doppler frequencies is of great significance. Inspired by this characteristic, in this work, time–frequency analysis methods are adopted to retrieve the time-varying Doppler frequencies, and to generate high-quality ISAR images. However, for classical time–frequency analysis methods, e.g., short-time Fourier transform (STFT), WVD, and so on, the Doppler frequencies are modeled as low-order signals, resulting in some imperfections in the ISAR images, such as cross-term interference or low-resolution characteristics.

In this work, to retrieve the structure of non-cooperative targets with time-varying characteristics, an efficient ISAR imaging approach combining HoSST with MMSR is proposed. First, the geometry and signal models of non-cooperative space targets with complex motion are established. Second, the echoes in each range bin are modeled as multi-component phase signals after correcting the translational migration and migration through range cells (MTRCs). Additionally, the time–frequency analysis (TFA) method based on HoSST is utilized to obtain the time–frequency signal along the azimuth dimension, where the coarse ISAR image is obtained, followed by an enhancement of the image using the MMSR method. Finally, both simulated and measured data experiments are used to validate the effectiveness and robustness of the proposed method.

Up to now, the two-dimensional ISAR images of targets can be obtained. However, the structure information of two-dimensional ISAR images is deficient compared with that of three-dimensional ISAR images. In addition, the generation of two-dimensional images is heavily dependent on the radar line of sight, which is inconvenient in real applications. Therefore, as a promising research direction, three-dimensional ISAR imaging approach designs for non-cooperative targets under low-SNR conditions will receive increasing attention. As a continuation of this work, in the future, three-dimensional ISAR imaging for non-cooperative space targets is urgent.

6. Conclusions

In this paper, an effective ISAR imaging method for non-cooperative space targets based on high-order synchrosqueezing transform (HoSST) and MMSR is proposed. First, the geometry and signal model of non-cooperative space targets are established. Second, the echoes in each range bin are modeled as multi-component polynomial phase signals (MCPPSs) after conducting a translational compensation operation. Additionally, the time–frequency analysis (TFA) method based on HoSST is utilized to obtain the time–frequency signal along the azimuth direction, where the coarse ISAR image is obtained based on the quality indicator, followed by an enhancement of the image using MMSR. Finally, both simulated and real measured data are utilized to verify the effectiveness of the proposed approach.

Author Contributions: Conceptualization, Z.Y.; Methodology, Z.Y.; Software, D.L.; Validation, C.Z.; Formal analysis, Z.Y. and X.X.; Investigation, Z.Y., C.Z. and D.L.; Data curation, Z.Y. and D.L.; Writing—original draft, Z.Y.; Writing—review & editing, C.Z. and X.X.; Visualization, D.L. and X.X.; Supervision, C.Z. and D.L.; Project administration, C.Z.; Funding acquisition, X.X. All authors have read and agreed to the published version of the manuscript.

Funding: This work was supported in part by the Natural Science Foundation of Chongqing, China, grant No. CSTB2022NSCQ-BHX0713; in part by the National Key Research and Development Program of China under Grant 2021YFC3001903; in part by the National Natural Science Foundation of China under Grants U2133217 and 61971037; in part by the Foundation of China State Construction Engineering Corporation (CSCEC-2022-Z-4); and by the National Natural Science Foundation of China (62101036).

Institutional Review Board Statement: Not applicable.

Informed Consent Statement: Not applicable.

Data Availability Statement: Not applicable.

Conflicts of Interest: The authors declare no conflict of interest.

References

1. Lazarov, A.; Minchev, C. ISAR geometry, signal model, and image processing algorithms. *IET Radar Sonar Navig.* **2017**, *11*, 1425–1434. [[CrossRef](#)]
2. Yang, Z.; Li, D.; Tan, X.; Liu, H.; Liu, Y.; Liao, G. ISAR Imaging for Maneuvering Targets with Complex Motion Based on Generalized Radon-Fourier Transform and Gradient-Based Descent under Low SNR. *Remote Sens.* **2021**, *13*, 2198. [[CrossRef](#)]
3. Bai, X.; Tao, R.; Wang, Z.; Wang, Y. ISAR Imaging of a Ship Target Based on Parameter Estimation of Multicomponent Quadratic Frequency-Modulated Signals. *IEEE Trans. Geosci. Remote Sens.* **2014**, *52*, 1418–1429. [[CrossRef](#)]
4. Wang, B.; Cha, H.; Zhou, Z.; Tang, H.; Sun, L.; Du, B.; Zuo, L. An Iterative Phase Autofocus Approach for ISAR Imaging of Maneuvering Targets. *Electronics* **2021**, *10*, 2100. [[CrossRef](#)]
5. Yang, Z.; Li, D.; Tan, X.; Liu, H.; Xu, L.; Liao, G. An Efficient ISAR Imaging Approach for Highly Maneuvering Targets Based on Subarray Averaging and Image Entropy. *IEEE Trans. Geosci. Remote Sens.* **2022**, *60*, 5102113. [[CrossRef](#)]
6. Chen, C.-C.; Andrews, H.C. Target-Motion-Induced Radar Imaging. *IEEE Trans. Aerosp. Electron. Syst.* **1980**, *AES-16*, 2–14. [[CrossRef](#)]
7. Chen, V.C.; Miceli, W.J. Time-varying spectral analysis for radar imaging of manoeuvring targets. *IEE Proc. Radar Sonar Navig.* **1998**, *145*, 262–268. [[CrossRef](#)]
8. Wang, Y.; Kang, J.; Jiang, Y. ISAR Imaging of Maneuvering Target Based on the Local Polynomial Wigner Distribution and Integrated High-Order Ambiguity Function for Cubic Phase Signal Model. *IEEE J. Sel. Top. Appl. Earth Obs. Remote Sens.* **2014**, *7*, 2971–2991. [[CrossRef](#)]
9. Wang, Y.; Jiang, Y. ISAR Imaging of a Ship Target Using Product High-Order Matched-Phase Transform. *IEEE Geosci. Remote Sens. Lett.* **2009**, *6*, 658–661. [[CrossRef](#)]
10. O’Shea, P.; Wiltshire, R.A. A New Class of Multilinear Functions for Polynomial Phase Signal Analysis. *IEEE Trans. Signal Process.* **2009**, *57*, 2096–2109. [[CrossRef](#)]
11. Zheng, J.; Su, T.; Zhang, L.; Zhu, W.; Liu, Q.H. ISAR Imaging of Targets With Complex Motion Based on the Chirp Rate–Quadratic Chirp Rate Distribution. *IEEE Trans. Geosci. Remote Sens.* **2014**, *52*, 7276–7289. [[CrossRef](#)]
12. Wang, Y.; Jiang, Y. Inverse Synthetic Aperture Radar Imaging of Maneuvering Target Based on the Product Generalized Cubic Phase Function. *IEEE Geosci. Remote Sens. Lett.* **2011**, *8*, 958–962. [[CrossRef](#)]

13. Lv, Q.; Su, T.; He, X. An ISAR Imaging Algorithm for Nonuniformly Rotating Targets With Low SNR Based on Modified Bilinear Parameter Estimation of Cubic Phase Signal. *IEEE Trans. Aerosp. Electron. Syst.* **2018**, *54*, 3108–3124. [[CrossRef](#)]
14. Du, Y.; Jiang, Y.; Wang, Y.; Zhou, W.; Liu, Z. ISAR Imaging for Low-Earth-Orbit Target Based on Coherent Integrated Smoothed Generalized Cubic Phase Function. *IEEE Trans. Geosci. Remote Sens.* **2020**, *58*, 1205–1220. [[CrossRef](#)]
15. Xia, X.-G.; Wang, G.; Chen, V.C. Quantitative SNR analysis for ISAR imaging using joint time-frequency analysis-Short time Fourier transform. *IEEE Trans. Aerosp. Electron. Syst.* **2002**, *38*, 649–659. [[CrossRef](#)]
16. Kim, K.T.; Choi, I.S.; Kim, H.T. Efficient radar target classification using adaptive joint time-frequency processing. *IEEE Trans. Antennas Propag.* **2000**, *48*, 1789–1801. [[CrossRef](#)]
17. Thayaparan, T.; Brinkman, W.; Lampropoulos, G. Inverse synthetic aperture radar image focusing using fast adaptive joint time-frequency and three-dimensional motion detection on experimental radar data. *IET Signal Process* **2010**, *4*, 382–394. [[CrossRef](#)]
18. Xing, M.D.; Wu, R.; Li, Y.; Bao, Z. New ISAR imaging algorithm based on modified Wigner-Ville distribution. *IET Radar Sonar Navigat.* **2009**, *3*, 70–80. [[CrossRef](#)]
19. Zheng, B.; Sun, C.; Xing, M. Time-frequency approaches to ISAR imaging of maneuvering targets and their limitations. *IEEE Trans. Aerosp. Electron. Syst.* **2001**, *37*, 1091–1099. [[CrossRef](#)]
20. Wu, Y.; Munson, D.C. Wide-angle ISAR passive imaging using smoothed pseudo Wigner-Ville distribution. In Proceedings of the 2001 IEEE Radar Conference (Cat. No.01CH37200), Atlanta, GA, USA, 3 May 2001; pp. 363–368. [[CrossRef](#)]
21. Wang, Y.; Jiang, Y. ISAR Imaging of Maneuvering Target Based on the L-Class of Fourth-Order Complex-Lag PWVD. *IEEE Trans. Geosci. Remote Sens.* **2010**, *48*, 1518–1527. [[CrossRef](#)]
22. Zang, B.; Zhu, M.; Zhou, X.; Zhong, L. Application of S-Transform in ISAR Imaging. *Electronics* **2019**, *8*, 676. [[CrossRef](#)]
23. Li, D.; Liu, H.; Gui, X.; Zhang, X. An Efficient ISAR Imaging Method for Maneuvering Target Based on Synchrosqueezing Transform. *IEEE Antennas Wirel. Propag. Lett.* **2016**, *15*, 1317–1320. [[CrossRef](#)]
24. Kong, L.; Zhang, W.; Zhang, S.; Zhou, B. Radon transform and the modified envelope correlation method for ISAR imaging of multi-target. In Proceedings of the 2010 IEEE Radar Conference, Arlington, VA, USA, 10–14 May 2010; pp. 637–641. [[CrossRef](#)]
25. Wang, J.; Kasilingam, D. Global range alignment for ISAR. *IEEE Trans. Aerosp. Electron. Syst.* **2003**, *39*, 351–357. [[CrossRef](#)]
26. Li, X.; Liu, G.; Ni, J. Autofocusing of ISAR images based on entropy minimization. *IEEE Trans. Aerosp. Electron. Syst.* **1999**, *35*, 1240–1252. [[CrossRef](#)]
27. Cai, J.; Martorella, M.; Chang, S.; Liu, Q.; Ding, Z.; Long, T. Efficient Nonparametric ISAR Autofocus Algorithm Based on Contrast Maximization and Newton’s Method. *IEEE Sens. J.* **2021**, *21*, 4474–4487. [[CrossRef](#)]
28. Perry, R.P.; DiPietro, R.C.; Fante, R.L. SAR imaging of moving targets. *IEEE Trans. Aerosp. Electron. Syst.* **1999**, *35*, 188–200. [[CrossRef](#)]
29. Pham, D.-H.; Meignen, S. High-Order Synchrosqueezing Transform for Multicomponent Signals Analysis—With an Application to Gravitational-Wave Signal. *IEEE Trans. Signal Process.* **2017**, *65*, 3168–3178. [[CrossRef](#)]
30. Liu, W.; Cao, S.; Wang, Z.; Jiang, K.; Zhang, Q.; Chen, Y. A Novel Approach for Seismic Time-Frequency Analysis Based on High-Order Synchrosqueezing Transform. *IEEE Geosci. Remote Sens. Lett.* **2018**, *15*, 1159–1163. [[CrossRef](#)]
31. Noviello, C.; Fornaro, G.; Braca, P.; Martorella, M. Fast and Accurate ISAR Focusing Based on a Doppler Parameter Estimation Algorithm. *IEEE Geosci. Remote Sens. Lett.* **2017**, *14*, 349–353. [[CrossRef](#)]
32. Wang, J.; Kasilingam, D.; Liu, X.; Zhou, Z. ISAR minimum-entropy phase adjustment. In Proceedings of the 2004 IEEE Radar Conference (IEEE Cat. No.04CH37509), Philadelphia, PA, USA, 29 April 2004; pp. 197–200. [[CrossRef](#)]
33. Martorella, M.; Berizzi, F.; Haywood, B. Contrast maximization based technique for 2-D ISAR autofocusing. *IEE Proc. Radar Sonar Navigat.* **2005**, *152*, 253–262. [[CrossRef](#)]
34. Liu, L.; Zhou, F.; Tao, M.L.; Sun, P.; Zhang, Z.J. Adaptive translational motion compensation method for ISAR imaging under low SNR based on particle swarm optimization. *IEEE J. Sel. Topics Appl. Earth Observ. Remote Sens.* **2015**, *8*, 5146–5157. [[CrossRef](#)]
35. Wang, B.B.; Xu, S.Y.; Wu, W.Z.; Hu, P.J.; Chen, Z.P. Adaptive ISAR imaging of maneuvering targets based on a modified Fourier transform. *Sensors* **2018**, *18*, 1370. [[CrossRef](#)] [[PubMed](#)]
36. Lv, Y.; Wu, Y.; Wang, H.; Qiu, L.; Jiang, J.; Sun, Y. An Inverse Synthetic Aperture Ladar Imaging Algorithm of Maneuvering Target Based on Integral Cubic Phase Function-Fractional Fourier Transform. *Electronics* **2018**, *7*, 148. [[CrossRef](#)]
37. Ruan, H.; Wu, Y.; Jia, X.; Ye, W. Novel ISAR Imaging Algorithm for Maneuvering Targets Based on a Modified Keystone Transform. *IEEE Geosci. Remote Sens. Lett.* **2014**, *11*, 128–132. [[CrossRef](#)]

Disclaimer/Publisher’s Note: The statements, opinions and data contained in all publications are solely those of the individual author(s) and contributor(s) and not of MDPI and/or the editor(s). MDPI and/or the editor(s) disclaim responsibility for any injury to people or property resulting from any ideas, methods, instructions or products referred to in the content.